ROYAL SOCIETY
OF CHEMISTRY

PAPER

Check for updates

In situ grown hierarchical NiO nanosheet@nanowire arrays for high-performance electrochromic energy storage applications†

Shangzhi Yao,[ab] Yong Zhang, [ID] *[ab] Jingyi Cai,[ab] Yong Hong,[c] Yan Wang, [ID] [ab] Jiewu Cui, [ID] [ab] Xia Shu,[ab] Jiaqin Liu, [ID] [ad] Hark Hoe Tan[e] and Yucheng Wu [ID] *[ab]

Electrodes with hierarchical nanoarchitectures could promote electrochemical properties due to their largely exposed active sites and quick charge transfer. Herein, *in situ* grown hierarchical NiO nanosheet@nanowire films are reported by a one-step hydrothermal process followed by heat treatment. The unique NiO hierarchical nanostructures, which are composed of NiO nanowires grown on the surface of a nanosheet array, show improved electrochromic properties such as large optical modulation in different light regions (95% at 550 nm and 50.6% at 1000 nm), fast color change (9.8/5.4 s) and better coloring efficiency (91.2 cm^2 C^{-1}) with long-term cycling properties (82.2% after 700 cycles). Simultaneously, the hierarchical nanostructures possess optimal areal capacitance (117.2 mF cm^{-2}), rate performance and cycling properties. The enhanced electrochemical properties are due to the pretreated seed layer and the synergistic effect between the unique *in situ* grown ultrathin nanowire and the underlying vertical nanosheet layer which can strengthen the mechanical adhesion of the nanoarray film to the substrate and make both nanosheets and nanowires more exposed to the electrolyte, enhancing charge transfer and mass diffusion. This work provides a promising pathway towards developing high quality electrochromic energy storage devices.

Introduction

Electrochromic smart windows are increasingly used due to their ability to adjust the transmittance of visible and NIR light into city buildings under different applied voltages to regulate the ion injection/extraction behavior.[1–6] Simultaneously, the special electrochromic process can also lead to relevant pseudocapacitive behaviors which enable the material to possess a superior energy storage performance.[7–12] The green energy technology can improve building lighting and heating and thus can reduce energy consumption.[13–20]

Among the many electrochromic energy storage materials, NiO has become one of the most attractive candidates due to its promising modulation range, excellent electrochromic

efficiency, high theoretical specific capacitance and low cost. Nevertheless, the low reaction kinetics, poor bleached-state transparency and inevitable degradation during cycling in alkaline environments limit its development.[21–25]

It is well known that three-dimensional hierarchical complex nanostructures can avoid numerous shortcomings in the electrochemical reaction process.[26–31] Both quick electron transfer of the inner body and the more exposed area of the external branches can allow uniform interfacial/chemical distribution and fast ion and electron transfer at the nanoscale. For instance, Duan *et al.* reported three-ordered Co_3O_4 nanostructures which showed better super-capacitive properties (5.44 F cm^{-2} at 5 mA cm^{-2}), much better than those of the individual arrays (Co_3O_4 nanostructures).[32] Tu *et al.* synthesized a porous $NiCo_2O_4$ nanoflake@nanowire array in two steps (hydrothermal procedure and heat treatment). The unique array shows a high super-capacitive performance of 891 F g^{-1} at 1 A g^{-1} with good long-term stability.[33] Zhao *et al.* synthesized a typical rGO/NiO heterostructure film by integrating $Ni(OH)_2$ and GO followed by an annealing process, obtaining better capacitance properties (269 mF cm^{-2} at 0.5 mA cm^{-2}) and a large color contrast of 53% at 630 nm.[34] Although several hierarchical structures such as nanosheets/wires or nanowires/sheets have been reported, they are generally prepared by a two-step synthesis, *i.e.*, the primary nanostructure is first prepared as a skeleton, and the secondary structure is subsequently

a School of Materials Science and Engineering, Hefei University of Technology, Hefei, 230009, China. E-mail: zhangyong.mse@hfut.edu.cn; ycwu@hfut.edu.cn

b Key Laboratory of Advanced Functional Materials and Devices of Anhui Province, Hefei, 230009, China

c School of Mechanical Engineering, Shanghai Dianji University, Shanghai 201306, China

d Institute of Industry & Equipment Technology, Hefei University of Technology, No.193 Tunxi Road, Hefei, Anhui 230009, China

e Department of Electronic Materials Engineering, Research School of Physics and Engineering, The Australian National University, Canberra, ACT 2601, Australia

† Electronic supplementary information (ESI) available. See https://doi.org/10.1039/d2na00505k
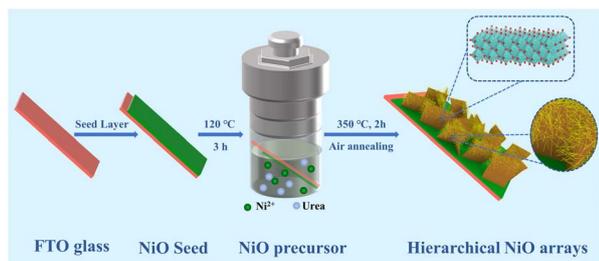
Scheme 1 Schematic diagram of the experiment process of hierarchical NiO nanostructures.

compounded on the skeleton by adopting other synthesis conditions or methods.[35–39] Adopting multiple/different preparation conditions or methods can inevitably increase the variability and uncertainties of the synthesis process.[7,11,40–45]

Herein, an *in situ* grown hierarchical NiO nanosheet@nanowire array film was fabricated on FTO glass substrates by one-step hydrothermal treatment followed by a heat treatment process. The unique NiO arrays possess improved electrochromic energy storage properties such as ultra-high optical modulation in different light regions, exceptional cycling stability, optimized coloring efficiency and high areal capacitance (Scheme 1).

Results and discussion

Fig. 1 shows the high-resolution FESEM images of the NiO samples hydrothermally treated for different times. In the initial 1 h reaction, the precursor material exhibits a vertical nanosheet structure on FTO (Fig. 1a). The nanosheet has a length of ~300 nm, a height of ~200 nm, and a thickness of ~20 nm. After reaction for 3 h, a large number of ultrafine nanowires (2–5 nm in diameter) begin to grow on the vertical nanosheets (Fig. 1b and S1a†). The average length is around 145 nm (Fig. S2†). As the reaction time rises to 6 h, more nanowires grow from various parts of the nanosheet, and gradually become longer and begin to interweave (Fig. 1c). With the hydrothermal treatment time further prolonging to 9 h, the upper nanowires become more and even longer to the extent that they cover the nanosheets completely (Fig. 1d). The obtained hierarchical structure possesses an underlying vertical nanosheet structure with a reasonable spacing between the nanosheets and the upper nanowires, which will make more active surface sites exposed and promote charge transfer in the electrolyte to facilitate the electrochemical process. Fig. 1e and f exhibit the TEM and corresponding HRTEM images of NiO-3 h. The crystalline lattice fringes with a distance of 0.204 nm and 0.240 nm can be ascribed to the (200) and (111) planes of cubic NiO, respectively. As shown in Fig. S1b,† these diffraction rings can match well with the (220), (200), and (111) crystal faces. The energy dispersive spectroscopy maps of NiO clearly evidence that Ni and O distribute evenly.[11,40,46]

To further understand the growth process of the hierarchical structure, FESEM images of the NiO precursors are shown in Fig. S3,† which show similar morphologies and variation trends
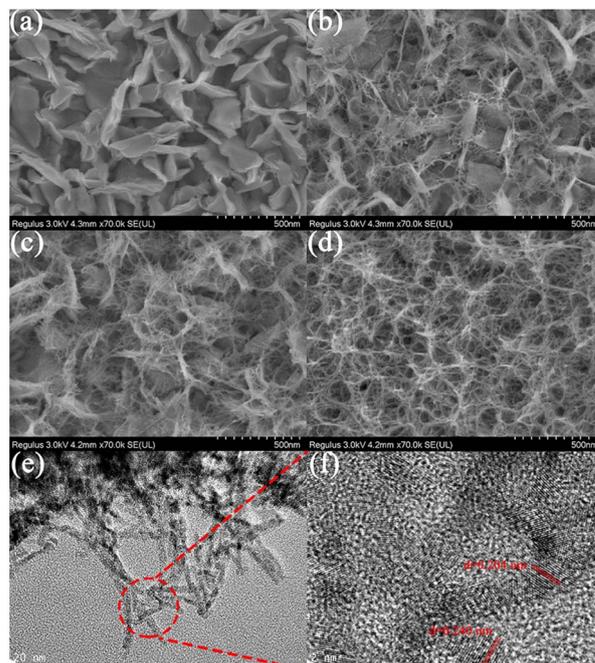

Fig. 1 (a–d) High-resolution FESEM images of NiO-1 h, NiO-3 h, NiO-6 h and NiO-9 h. (e) TEM and (f) corresponding HRTEM images of NiO-3 h.

to the annealed NiO films, suggesting that the NiO film can well inherit the morphology of the precursor which would not be affected by the post-treatment. Herein, we propose a possible formation mechanism of the unique hierarchical nanostructures as shown in Fig. 2, which can be described as the Ostwald ripening and Oriented attachment process. In the initial stage, plenty of small nucleated particles will start to form in the FTO surface. Simultaneously, when the seed layer is pre-prepared, the surface of the FTO is scattered with many sites of high nickel concentration, which can serve as nucleation sites to form large-sized nanoparticles. According to Yu's work, when the size of nanoparticles exceeds 5 nm, Ostwald ripening can occur where small nucleated particles dissolve and larger particles (seed layer) grow by ingesting the mass of small particles, which minimizes the total interfacial free energy.[47] Subsequently, the precursor tends to form a vertical nanosheet structure on the FTO surface. When the nanosheet structure is formed after the nucleation and growth along the seed layer based on the Ostwald ripening mechanism, secondary
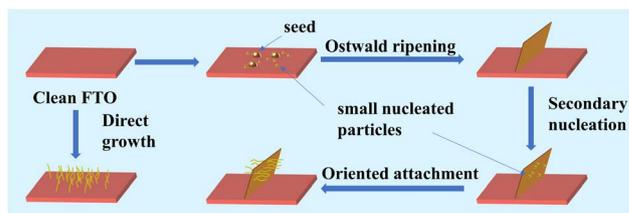

Fig. 2 Schematic diagram of the growth mechanism of the NiO hierarchical nanostructures.

nucleation would preferentially occur on the surface of the obtained nanosheets due to the depletion of the seed layer. Owing to the fine control of the reactant concentration and reaction parameters, the generated tiny nuclei favor the oriented attachment (OA) growth. The growth mechanism would induce the "one-by-one" connected growth of ultrasmall nuclei to form ultrafine nanowire structure. Simultaneously, secondary nucleation takes place more preferentially on the nanosheet surface than on the substrate surface due to the lower nucleus/particle interfacial energy. The nanosheet can act as a skeleton and also guide the *in situ* growth of the nanowire. As for the FTO substrate without the seed layer treatment, the nucleation process of the precursors is similar to the above-mentioned secondary nucleation stage. The precursors nucleate on the surface of the untreated FTO and subsequently grow into nanowires without the induction of a seed layer (Fig. S4a†). The cross-sectional SEM images of NiO-9 h show that the upper nanowires and the underlying nanosheets co-exist in the hierarchical structure in Fig. S5.† The morphology evolution observation of the NiO samples with increasing reaction time evidences the above-mentioned two-stage growth mechanism of the hierarchical nanostructures which involves the Ostwald ripening and Oriented attachment stage, respectively.

In order to determine the suitable annealing temperature before preparation of the NiO thin film, we carried out a TGA test of the precursor powder. The first weight loss from ambient temperature to 260 °C corresponds to adsorbed water on the precursor as shown in Fig. S6.† Then, the Ni precursor will convert to NiO until the temperature reaches 350 °C. It should be noted that NiO which is obtained at this point is not stoichiometric nickel oxide, because the resulting product is still being thermally decomposed for a subsequent period of time until stoichiometric nickel oxide is formed.[48,49] Moreover, the resistivity of FTO increases above 350 °C, so we choose this temperature as the optimal annealing temperature. Since the signal of the film was covered by the FTO substrates, all samples

were scraped from the substrate to collect the XRD patterns. Fig. 3a exhibits the XRD patterns of synthesized NiO samples which display three prominent diffraction peaks at 37.2°, 43.4°, and 62.8°, indexed to the (111), (200) and (220) planes of cubic NiO (PDF# 47-1049), respectively. No other distinct peaks exist, implying the absence of new impurity phases.[50–52] Interestingly, the peak intensity of all NiO samples is high, demonstrating their strong crystallinity. XPS was performed to analyze the surficial compositions and corresponding element states of NiO-3 h. The obtained survey spectrum exhibits the presence of Ni, O and C and absence of other impurities in Fig. 3b. In Fig. 3c, two peaks at binding energies of 853.4 eV and 855.1 eV can represent Ni^{2+} and Ni^{3+}, respectively. The latter peak possesses a large area, suggesting more Ni^{3+} content. Ni^{2+} and Ni^{3+} co-exist in the NiO-3h film, and since Ni^{3+} is an electrochromic active factor, more Ni^{3+} content can help improve the electrochromic performance.[22,53] In the O 1s core level, two peaks at 530.7 and 528.8 eV can stand for Ni–O and O_{vac}, respectively (Fig. 3d). Notably, the peak at about 532.3 eV represents the adsorbed water.[25] The electron paramagnetic resonance (EPR) spectrum of the NiO-3 h film is presented in Fig. S7† where a peak corresponding to an EPR signal at $g = 2.003$ is observed, which stands for existing oxygen vacancies.[54–56]

Before the electrochemical tests, an essential activation process was carried out (Fig. S8†). To explore the electrochromic performance of NiO samples, the transmittance spectra of colored and bleached states were investigated (Fig. 4a–d). The NiO-3 h film shows higher transmittance both in visible and NIR regions in the bleached state. Obviously, the transmittance decreases considerably and the sample turns dark brown in the bleached state (Fig. S9†). Optical modulation (ΔT) is a crucial
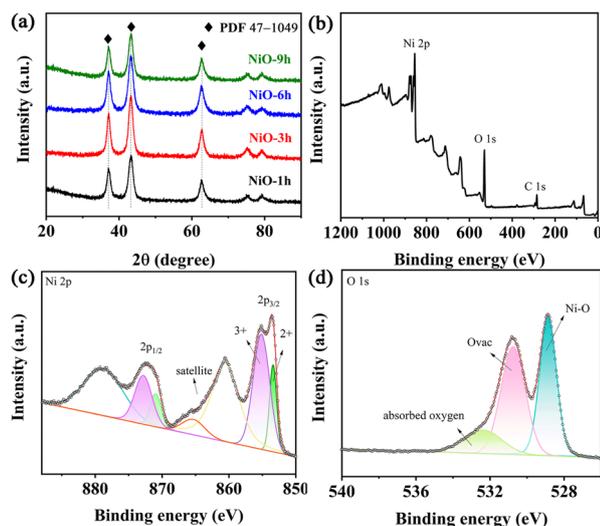

Fig. 3 (a) XRD patterns of the NiO samples. (b) XPS full survey spectrum, (c) Ni 2p and (d) O 1s of the NiO-3 h film.
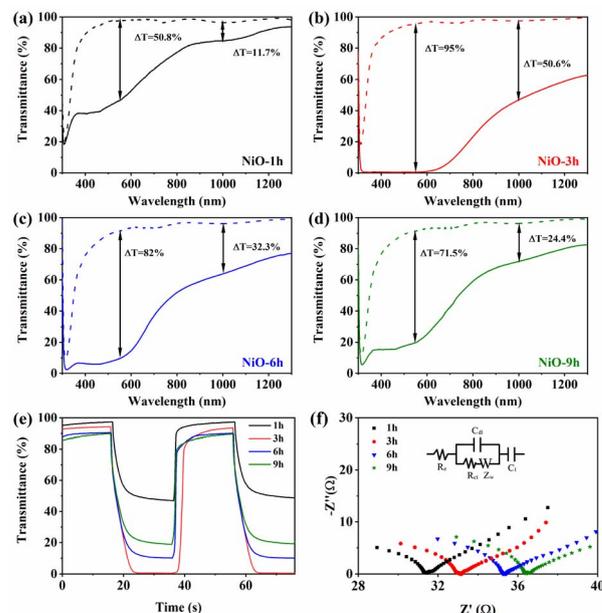

Fig. 4 Transmittance spectra of (a) NiO-1 h, (b) NiO-3 h, (c) NiO-6 h and (d) NiO-9 h. (e) Dynamic optical transmittance spectra of the synthesized NiO films. (f) EIS of the NiO films.

parameter in assessing the electrochromic performance, which means the difference of transmittance at bleached and colored states. Obviously, the NiO-3 h film shows a wide-band color contrast, and the corresponding optical modulation is 95% at 550 nm, compared to 50.8%, 82% and 71.5% for NiO-1 h, NiO-6 h and NiO-9 h, respectively. With increasing reaction time, the optical modulation increases and then decreases, reaching the maximum value at 3 h. Furthermore, it is surprising that NiO-3 h also has a good optical modulation in the NIR region (50.6% at 1000 nm), which is rarely reported for NiO samples in the literature. The introduction of oxygen vacancies may generate an impurity band between the valence band and conduction band in the NiO film, which decreases the band gap and makes the absorption peak shift to the longer wavelength region (red shift), thereby improving the light absorption in the NIR region.[57,58] Simultaneously, oxygen vacancies can reduce the energy required for an electron transition to the conduction band, which improves the electronic conductivity and provides better adsorption of oxhydryl for a further redox process, thus improving the electrochromic performance of the material.[59–62] According to Fig. S10,† the peak area of O_{vac} increases with the reaction time, implying a higher oxygen vacancy concentration. However, for electrochromic materials, more oxygen vacancies may lead to the increase of Ni^{2+} concentration, and decrease of Ni^{3+} with electrochromic activity, which is harmful to electrochromic performance. The *in situ* dynamic transmittance spectra were recorded to quantitatively assess the color change feature of the NiO sample as shown in Fig. 4e. The calculated bleaching and coloring times are 5.4 s and 9.8 s, respectively, which are close to those of other NiO films shown in Table S1.†

To further analyze the charge transport behavior of the obtained NiO samples, electrochemical impedance spectroscopy was performed as shown in Fig. 4f. The inset picture depicts the equivalent circuit, where R_{ct} and R_e stand for the charge transfer resistance and electrolyte resistance, respectively. Additionally, C_{dl} stands for the capacitance of the double capacitive layer. For the linear part, a steeper slope means faster ion diffusion. As shown in Table 1, the calculated R_{ct} of NiO-3 h is 24.53 Ω, implying its low charge transfer impedance. In addition, NiO-3 h has the largest C_{dl} value of 0.032 μF, indicating the largest electrochemically active area amongst the four samples. It can also be seen that NiO-3 h has the largest slope of the linear part, suggesting a fast mass diffusion. The electrical conductivity of the sample deteriorates with excessive reaction time, which is due to the increasing difficulty of electron diffusion from longer and more dense nanowires to the underlying nanosheets.[40,63]

Coloration efficiency (CE) plays a crucial part in assessing the electrochromic properties which can be evaluated by two formulas.

$$CE = \Delta OD/Q \tag{1}$$

$$\Delta OD = \log T_b/T_c \tag{2}$$

where ΔOD and Q stand for the optical density change and unit injected/extracted charge divided by the electrochemical reaction area, respectively. T_b and T_c stand for the corresponding transmittance in the bleached and colored state. The calculated CE values at 550 nm for the four NiO samples from Fig. 5a–d are 12.7, 91.2, 23.7 and 16.6 $cm^2\ C^{-1}$, respectively. The trend of the CE resembles that of the optical modulation. Generally, the coloring efficiency is relevant to the surface morphology. NiO-3 h exhibits a high coloring efficiency when a three-dimensional hierarchical structure with an ultra-high electrochemically active area is present, which also corroborates earlier results.[64,65]

CV measurements were performed to assess the charge storage ability. It is obvious that the enclosed area of NiO-3 h is significantly larger than that of the other NiO films as shown in Fig. 6a, indicating that NiO-3 h has a higher electrochemically active area, which coincides with the results from SEM and CE. Meanwhile, with the increase of hydrothermal time, the electrochemically active area of each sample first increased and subsequently decreased, reaching the maximum value at 3 h. Interestingly, such a variation law also applies to the C_{dl} value of the EIS impedance. Hence, we determine that NiO-3 h has the maximum electrochemically active area. Notably, based on the above analysis, further study of the variation of the active area will help to give a more profound indication of the variation of the electrochemical activity of samples with different morphologies, which will be carried out in future work. Fig. S11† further exhibits the CV curves of NiO-3 h at different scan rates. Two prominent peaks which can be ascribed to the existence of redox reaction of Ni^{2+} to Ni^{3+} appear in the films. With the scan rate increasing, both redox peaks show a shift to more positive and negative directions, respectively. Notably, the
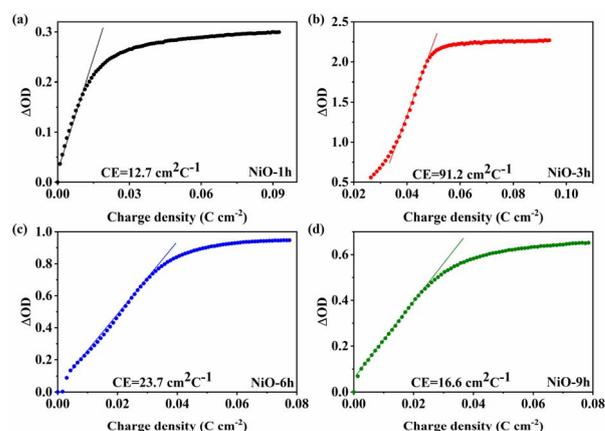
Table 1 EIS parameters of the NiO films calculated by the Zsimpwin software

Film	R_e (Ω)	C_{dl} (μF)	R_{ct} (Ω)
NiO-1 h	29.69	0.030	22.71
NiO-3 h	30.77	0.032	24.53
NiO-6 h	27.58	0.027	27.20
NiO-9 h	29.00	0.025	29.72

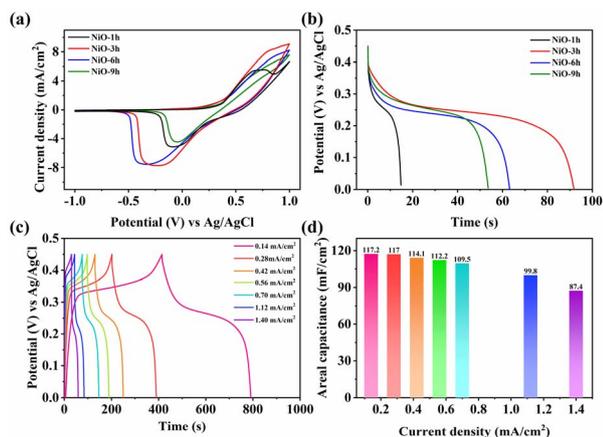**Fig. 5** (a–d) The optical density changes with charge density of the NiO films.

Fig. 6 (a) CV curves at a scan rate of 0.005 V s^{-1} and (b) galvanostatic discharge curves of the synthesized NiO films. (c) Galvanostatic charge/discharge curves and (d) corresponding calculated areal capacitance of NiO-3 h at different current densities.

shape of the CV curves basically remains unchanged, implying outstanding electrochemical reversibility. The reversible redox process can also provide potential super-capacitive performance. In addition, the diffusion and pseudocapacitance control processes can be identified due to the following relation:

$$\log i = b \times \log \nu + \log a \tag{3}$$

where ν is the scan rate, and a and b are adjustable parameters (Fig. S12†). Usually, the b value equals 0.5 representing a diffusion-controlled process, while the b value of 1.0 suggests a pseudocapacitance-controlled process. The calculated b values of the obtained NiO thin film are shown in Fig. S12.† The b value of NiO-3 h is 0.52, which indicates that the process is mostly dominated by a diffusion-controlled process. Fig. 6b exhibits the discharge curves of the NiO films at 0.56 mA cm^{-2}. NiO-3 h shows the longest discharging time among the obtained NiO samples due to the large electrochemically active surface. Further GCD investigations of NiO-3 h from 0 to 0.45 V were performed.

Fig. 6c shows that the charge–discharge curves are symmetrical, meaning good reversibility, consistent with CV analysis. NiO-3 h possesses the highest areal capacitance performance (117.2 mF cm^{-2} at 0.14 mA cm^{-2}). The areal capacitance can still remain at 74.6% even when increasing the current density to tenfold, exhibiting optimal rate capability of the hierarchical nanofilm (Fig. 6d). Notably, the GCD curve demonstrates that the NiO-3 h film exhibits distinct characteristics of a battery-type supercapacitor. Unlike the classical double-layer supercapacitor, two distinct plateaus appear when charging and discharging, representing the generation of redox processes accompanying the phase transition process, that is, Ni^{2+}/Ni^{3+} redox processes. The battery-type supercapacitor feature based on the electrochemical redox process contributes to the enhanced super-capacitance performance and may find promising potential for electrochromic energy storage.

Repetitive charge/discharge measurements were performed at 0.42 mA cm^{-2} for 1000 cycles to assess their cycle performance. Fig. S13† shows that the NiO-3 h electrode retained 58.5% of its initial capacitance. The sample loses 39% of its initial value after the first 700 cycles but only an additional 2.5% is lost in the next 300 cycles. Nevertheless, the sample maintains a high coulombic efficiency of 97%. This is ascribed to the robust hierarchical arrays of the electrodes, which contribute to the ion movement in electrolyte.[44,66,67]

As for electrochromic application, long-term cycling stability is also a crucial part to assess the durability of the material. In Fig. 7a, NiO-3 h was cycled for 700 times between −1.0 V and +1.0 V using chronoamperometry measurements. During cycling, the injection/extraction current of the film decreases slightly. Meanwhile, the optical modulation of the films maintains a retention of 88.1% after 500 cycles and 82.2% after 700 cycles as shown in Fig. 7b, which has been considerably improved in comparison with previous reports. To investigate the material state after cycling, we performed CV tests for each cycle number in Fig. 7c. The enclosed area and observed peak current of the CV curve gradually decrease with increasing number of cycles, implying a decrease in electrochemical activity. In summary, NiO-3 h shows advanced electrochromic energy storage performance in comparison with previous reports. The detailed data of some reported NiO films are listed in Table S2.†

The exact mechanism of electrochromism in NiO in alkaline environments is still controversial, but it is well accepted that phase change due to the reversible conversion of Ni^{2+} to Ni^{3+} is a key factor. Therefore, Raman tests were carried out on the films in the initial, colored and bleached states as shown in Fig. 7d. For the initial state, the peak at 1095 cm^{-1} can stand for the 2LO phonon modes of NiO.[68] When the film is in the coloring state, the peaks of NiO disappear, while a peak at 470 cm^{-1} which can stand for the stretching vibration of the Ni–O–OH bond arises. The result shows that NiO is oxidized to NiOOH during the coloring process. Moreover, the bleached film shows
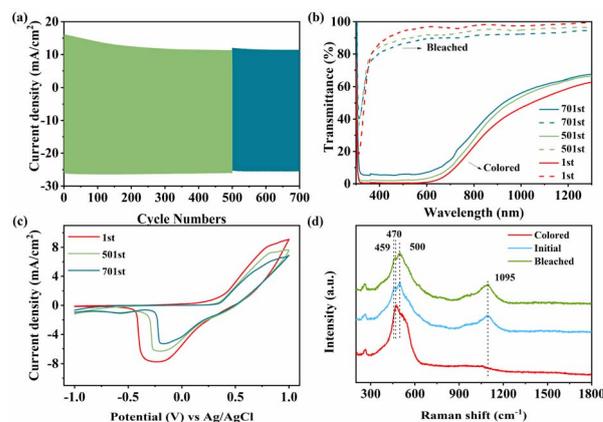

Fig. 7 (a) Current data of NiO-3 h before and after 700 cycles at 550 nm. (b) Transmittance spectra and (c) CV curves of NiO-3 h before and after 700 cycles. (d) Raman spectra of the initial state, bleached and colored state for the NiO-3 h sample.

two peaks at 459 and 500 cm^{-1} referring to the A$_{1g}$ stretching modes in Ni(OH)$_2$. Raman measurements were further performed on the samples after 700 cycles, as shown in Fig. S14a.† The characteristic spectrum of the colored film exhibits two peaks at 474 and 557 cm^{-1} attributed to the e$_g$ bending vibration and A$_{1g}$ stretching vibrational modes in NiOOH, respectively.[69–71] Compared to the uncycled colored state film, the peak of the cycled film is sharper and a characteristic peak located at 550 cm^{-1} appears, indicating an increased NiOOH concentration. Moreover, in the bleached state, the broad peak at 1095 cm^{-1} is lower in intensity than that of the initial bleached film, implying a lower amount of NiO. The peak at 500 cm^{-1} refers to Ni(OH)$_2$, which is prominent after 700 cycles. Simultaneously, the observed cycled XPS peak shifts toward higher binding energy, suggesting the formation of new higher valence Ni ions (Fig. S14b†). Based on the discussion above, the electrochromic mechanism of the NiO film can be concisely summarized as two steps:

$$NiO + OH^- \rightarrow NiOOH + e^- \qquad (4)$$

$$NiOOH + H_2O \leftrightarrow Ni(OH)_2 + OH^- \qquad (5)$$
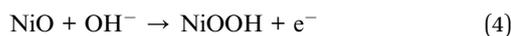
In the beginning of the coloring and bleaching cycle, the electrochromic reaction of the film is dominated by reaction (4), in which OH$^-$ is injected into the film and combines with NiO to form NiOOH to release an electron under positive bias. Then, NiOOH generated in the coloring process is gradually converted to Ni(OH)$_2$ in the bleaching process during the cycling, so that the amount of Ni(OH)$_2$ increases, *i.e.*, reaction (5) occurs. This also means that NiO is gradually converted to NiOOH during the whole cycling process, and the subsequent electrochromic process is achieved by the interconversion of transparent Ni(OH)$_2$ and dark brown NiOOH. The conversion of NiO to NiOOH is not completely reversible. NiOOH belongs to the hexagonal crystal lattice while NiO has a cubic crystal structure. Therefore, the cycling process will lead to the electrochromic degradation of the NiO films due to the mismatch in the crystal phase.

The optimized electrochromic and energy storage properties can be ascribed to the unique NiO nanosheet/nanowire hierarchical structure.[72–74] First, the pre-seed layer can induce the precursor to form the primary nanosheet structure, which can provide good mechanical bonding and improve charge transport between the electrochromic structure and the FTO glass. Second, compared with NiO-1 h, NiO-3 h possesses newly generated nanowires with more active sites involved in the electrochemical reaction, and the newly formed hierarchical nanostructures prompt the nanosheets and nanowires to be completely exposed to the electrolyte, thus enhancing the diffusion of ions as well as the penetration of the electrolyte for efficient utilization of the active sites. However, with the prolongation of hydrothermal time, nanowires become longer and tend to bunch up together, which would hinder the electrolyte penetration and ion exchange. The charge transport path from upper nanowires to underlying nanosheets also becomes longer, resulting in lower electrical conductivity. Therefore, too long reaction time would cause longer and crowder nanowires, deteriorating the electrochromic and electrocapacitive performance. Finally, the underlying nanosheets are interconnected to form a sheet-like network. These nanosheets support each other to form a stable structure. Moreover, the nanowires growing at the edges of the nanosheets are extremely thin and long, which allows sufficient three-dimensional space to mitigate volume expansion and structural disruption by the phase change due to ion injection/extraction during cycling, thus improving the long-term cycling properties.

Conclusions

In summary, hierarchical NiO nanosheet@nanowire films were prepared by a one-step hydrothermal method and subsequent heat treatment process. The morphology evolution observation evidences a two-stage growth mechanism which involves Ostwald ripening and an oriented attachment stage. The NiO film exhibits excellent electrochromic properties, superior color contrast in the visible and NIR region, quick color change, improved coloration efficiency, and optimal long-term cycling properties. Additionally, the unique hierarchical nanostructures possess high super-capacitive properties. The excellent electrochemical properties are ascribed to the pre-treated seed layer and unique three-dimensional hierarchical structure of underlying nanosheets and upper nanowires, which expose more active area, facilitate charge transfer and mass diffusion, and contribute to improved cycling stability. This work will inspire a development of using a facile and low-cost technique to fabricate hierarchical nanostructures for efficient electrochromic energy storage applications.

Conflicts of interest

There are no conflicts to declare.

Acknowledgements

References

1 Y. Huang, B. Wang, F. Chen, Y. Han, W. Zhang, X. Wu, R. Li, Q. Jiang, X. Jia and R. Zhang, *Adv. Opt. Mater.*, 2021, **10**, 2101783.

2 X. Li, K. Perera, J. He, A. Gumyusenge and J. Mei, *J. Mater. Chem. C*, 2019, **7**, 12761–12789.

3 A. Llordes, G. Garcia, J. Gazquez and D. J. Milliron, *Nature*, 2013, **500**, 323–326.

4 G. A. Niklasson and C. G. Granqvist, *J. Mater. Chem.*, 2007, **17**, 127–156.

5 J. Wang, X. Huo, M. Guo and M. Zhang, *J. Energy Storage*, 2022, **47**, 103597.

6 T. Y. Yun, X. Li, S. H. Kim and H. C. Moon, *ACS Appl. Mater. Interfaces*, 2018, **10**, 43993–43999.

7 G. Cai, X. Wang, M. Cui, P. Darmawan, J. Wang, A. L.-S. Eh and P. S. Lee, *Nano Energy*, 2015, **12**, 258–267.

8 J. Guo, M. Wang, G. Dong, Z. Zhang, Q. Zhang, H. Yu, Y. Xiao, Q. Liu, J. Liu and X. Diao, *Inorg. Chem.*, 2018, **57**, 8874–8880.

9 J. Mao, X. Duan and A. Yao, *Aust. J. Chem.*, 2019, **72**, 957–963.

10 I. Saadeddin, M. Suleiman, H. Salman, K. Zrikem, G. Song and A. Rougier, *Solid State Ionics*, 2019, **343**, 115129.

11 J. Shi, L. Lai, P. Zhang, H. Li, Y. Qin, Y. Gao, L. Luo and J. Lu, *J. Solid State Chem.*, 2016, **241**, 1–8.

12 C. Wu, Y. Yang, W. Feng, W. Song and R. Tan, *J. Alloys Compd.*, 2021, **862**, 158665.

13 S. Balasubramaniam, A. Mohanty, S. K. Balasingam, S. J. Kim and A. Ramadoss, *Nano-Micro Lett.*, 2020, **12**, 85.

14 T. S. Mathis, N. Kurra, X. Wang, D. Pinto, P. Simon and Y. Gogotsi, *Adv. Energy Mater.*, 2019, **9**, 1902007.

15 J. Zhou, S. Zhang, Y.-N. Zhou, W. Tang, J. Yang, C. Peng and Z. Guo, *Electrochem. Energy Rev.*, 2021, **4**, 219–248.

16 Y. Jiang, F. Guo, Y. Liu, Z. Xu and C. Gao, *SusMat*, 2021, **1**, 304–323.

17 M. Kang, H. Zhou, P. Wen and N. Zhao, *ACS Appl. Energ. Mater.*, 2021, **4**, 1619–1627.

18 X. Luo, S. Chen, T. Hu, Y. Chen and F. Li, *SusMat*, 2021, **1**, 211–240.

19 M. Rastgoo-Deylami and A. Esfandiar, *ACS Appl. Energy Mater.*, 2021, **4**, 2377–2387.

20 Z. Xu, W. Deng and X. Wang, *Electrochem. Energy Rev.*, 2021, **4**, 269–335.

21 G. Cai, J. Chen, J. Xiong, A. Lee-Sie Eh, J. Wang, M. Higuchi and P. S. Lee, *ACS Energy Lett.*, 2020, **5**, 1159–1166.

22 X. Guo, X. Diao and W. Wang, *Ceram. Int.*, 2021, **47**, 22240–22245.

23 Z. Luo, L. Liu, X. Yang, X. Luo, P. Bi, Z. Fu, A. Pang, W. Li and Y. Yi, *ACS Appl. Mater. Interfaces*, 2020, **12**, 39098–39107.

24 S. Xie, Y. Chen, Z. Bi, S. Jia, X. Guo, X. Gao and X. Li, *Chem. Eng. J.*, 2019, **370**, 1459–1466.

25 H. Zhang, S. Liu, T. Xu, W. Xie, G. Chen, L. Liang, J. Gao and H. Cao, *J. Mater. Chem. C*, 2021, **9**, 17427–17436.

26 Z. Li, Z. Yu, W. Wang, J. Hou, L. Gao, X. Gu and G. Su, *Mater. Chem. Phys.*, 2021, **269**, 124738.

27 D. Ma, G. Shi, H. Wang, Q. Zhang and Y. Li, *Nanoscale*, 2013, **5**, 4808–4815.

28 S. A. Mozaffari, S. H. Mahmoudi Najafi and Z. Norouzi, *Electrochim. Acta*, 2021, **368**, 137633.

29 L. Zhu, C. K. Nuo Peh, T. Zhu, Y.-F. Lim and G. W. Ho, *J. Mater. Chem. A*, 2017, **5**, 8343–8351.

30 W. Zhu, Z. Lu, G. Zhang, X. Lei, Z. Chang, J. Liu and X. Sun, *J. Mater. Chem. A*, 2013, **1**, 8327–8331.

31 S. I. Kim, J. S. Lee, H. J. Ahn, H. K. Song and J. H. Jang, *ACS Appl. Mater. Interfaces*, 2013, **5**, 1596–1603.

32 Q. Yang, Z. Lu, Z. Chang, W. Zhu, J. Sun, J. Liu, X. Sun and X. Duan, *RSC Adv.*, 2012, **2**, 1663–1668.

33 X. Y. Liu, Y. Q. Zhang, X. H. Xia, S. J. Shi, Y. Lu, X. L. Wang, C. D. Gu and J. P. Tu, *J. Power Sources*, 2013, **239**, 157–163.

34 J. Xue, H. Xu, S. Wang, T. Hao, Y. Yang, X. Zhang, Y. Song, Y. Li and J. Zhao, *Appl. Surf. Sci.*, 2021, **565**, 150512.

35 W. Chen, J. Wang, K. Y. Ma, M. Li, S. H. Guo, F. Liu and J. P. Cheng, *Appl. Surf. Sci.*, 2018, **451**, 280–288.

36 J. Liu, C. Cheng, W. Zhou, H. Li and H. J. Fan, *Chem. Commun.*, 2011, **47**, 3436–3438.

37 Y. Mao, Y. Cheng, J. Wang, H. Yang, M. Li, J. Chen, M. Chao, Y. Tong and E. Liang, *New J. Chem.*, 2016, **40**, 107–112.

38 X. Wang, B. Liu, J. Tang, G. Dai, B. Dong, L. Cao, R. Gao and G. Su, *Sol. Energy Mater. Sol. Cells*, 2019, **191**, 108–116.

39 S.-W. Zhang, B.-S. Yin, C. Liu, Z.-B. Wang and D.-M. Gu, *Chem. Eng. J.*, 2017, **312**, 296–305.

40 J. Xue, W. Li, Y. Song, Y. Li and J. Zhao, *J. Alloys Compd.*, 2021, **857**, 158087.

41 Y. Ren, X. Zhou, H. Zhang, L. Lei and G. Zhao, *J. Mater. Chem. C*, 2018, **6**, 4952–4958.

42 K.-H. Kim, S.-J. Jeong, B.-R. Koo and H.-J. Ahn, *Appl. Surf. Sci.*, 2021, **537**, 147902.

43 Y. He, T. Li, X. Zhong, M. Zhou, G. Dong and X. Diao, *Electrochim. Acta*, 2019, **316**, 143–151.

44 F. Khan, *Surfaces and Interfaces*, 2022, **29**, 101792.

45 A. Dewan, S. Haldar and R. Narayanan, *J. Solid State Electrochem.*, 2020, **25**, 821–830.

46 Y. Wei, F. Yan, X. Tang, Y. Luo, M. Zhang, W. Wei and L. Chen, *ACS Appl. Mater. Interfaces*, 2015, **7**, 21703–21711.

47 X. Chen, J. Wan, J. Wang, Q. Zhang, L. Gu, L. Zheng, N. Wang and R. Yu, *Adv. Mater.*, 2021, **33**, 2104764.

48 D. Wang, R. Xu, X. Wang and Y. Li, *Nanotechnology*, 2006, **17**, 979–983.

49 X. H. Xia, J. P. Tu, J. Zhang, X. L. Wang, W. K. Zhang and H. Huang, *Sol. Energy Mater. Sol. Cells*, 2008, **92**, 628–633.

50 A. Dewan, S. Sur, R. Narayanan and M. O. Thotiyl, *ChemElectroChem*, 2022, **9**, e202200001.

51 K. Song, L. Yuan, Z. Liu, H. Qiao, Y. Yu, X. Shen and X. Hu, *New J. Chem.*, 2022, **46**, 1601–1607.

52 X. Xia, Z. Ku, D. Zhou, Y. Zhong, Y. Zhang, Y. Wang, M. J. Huang, J. Tu and H. J. Fan, *Mater. Horizons*, 2016, **3**, 588–595.

53 H. Wang, B. Fan, Z. Luo, Q. Wu, X. Zhou and F. Wang, *Catal. Sci. Technol.*, 2021, **11**, 7632–7639.

54 S. Luo, X. Li, W. Gao, H. Zhang and M. Luo, *Sustainable Energy Fuels*, 2020, **4**, 164–170.

55 S. Visweswaran, R. Venkatachalapathy, M. Haris and R. Murugesan, *Appl. Phys. A*, 2020, **126**, 524.

56 J. Zheng, Y. Lyu, C. Xie, R. Wang, L. Tao, H. Wu, H. Zhou, S. Jiang and S. Wang, *Adv. Mater.*, 2018, **30**, 1801773.

57 D. Kong, J. Qi, D. Liu, X. Zhang, L. Pan and J. Zou, *Trans. Tianjin Univ.*, 2019, **25**, 340–347.

58 H. Liu, F. Zeng, Y. Lin, G. Wang and F. Pan, *Appl. Phys. Lett.*, 2013, **102**, 181908.

59 J. H. Lin, Y. T. Yan, T. X. Xu, C. Q. Qu, J. Li, J. Cao, J. C. Feng and J. L. Qi, *J. Colloid Interface Sci.*, 2020, **560**, 34–39.

60 H. Sun, Y. Zhao, K. Molhave, M. Zhang and J. Zhang, *Nanoscale*, 2017, **9**, 14431–14441.

61 Z. Xiao, Y. Wang, Y.-C. Huang, Z. Wei, C.-L. Dong, J. Ma, S. Shen, Y. Li and S. Wang, *Energy Environ. Sci.*, 2017, **10**, 2563–2569.

62 D. Yan, W. Wang, X. Luo, C. Chen, Y. Zeng and Z. Zhu, *Chem. Eng. J.*, 2018, **334**, 864–872.

63 C. Su, M. Qiu, Y. An, S. Sun, C. Zhao and W. Mai, *J. Mater. Chem. C*, 2020, **8**, 3010–3016.

64 P. Lei, J. Wang, P. Zhang, S. Liu, S. Zhang, Y. Gao, J. Tu and G. Cai, *J. Mater. Chem. C*, 2021, **9**, 14378–14387.

65 D. Ma, G. Shi, H. Wang, Q. Zhang and Y. Li, *J. Mater. Chem. A*, 2013, **1**, 684–691.

66 X. Huo, R. Li, J. Wang, M. Zhang and M. Guo, *Chem. Eng. J.*, 2022, **430**, 132821.

67 T. Wang, H. C. Chen, F. Yu, X. S. Zhao and H. Wang, *Energy Storage Mater.*, 2019, **16**, 545–573.

68 Y. Li, L. Hu, W. Zheng, X. Peng, M. Liu, P. K. Chu and L. Y. S. Lee, *Nano Energy*, 2018, **52**, 360–368.

69 O. Diaz-Morales, D. Ferrus-Suspedra and M. T. M. Koper, *Chem. Sci.*, 2016, **7**, 2639–2645.

70 S. Klaus, Y. Cai, M. W. Louie, L. Trotochaud and A. T. Bell, *J. Phys. Chem. C*, 2015, **119**, 7243–7254.

71 S. Yao, H. Wei, Y. Zhang, X. Zhang, Y. Wang, J. Liu, H. H. Tan, T. Xie and Y. Wu, *Catal. Sci. Technol.*, 2021, **11**, 264–271.

72 F. Li, M. Huang, J. Wang, J. Qu, Y. Li, L. Liu, V. K. Bandari, Y. Hong, B. Sun, M. Zhu, F. Zhu, Y. X. Zhang and O. G. Schmidt, *Energy Storage Mater.*, 2020, **27**, 17–24.

73 T. Wang, Y. Wang, J. Lei, K. J. Chen and H. Wang, *Exploration*, 2021, **1**, 20210178.

74 X. Zhao, X. Liu, F. Li and M. Huang, *J. Mater. Sci.*, 2019, **55**, 2482–2491.